Acta Materialia 275 (2024) 119994

Contents lists available at ScienceDirect

Acta Materialia

journal homepage: www.elsevier.com/locate/actamat

Full length article

An atomistic survey of shear coupling in asymmetric tilt grain boundaries and interpretation using the disconnections framework

Himanshu Joshi [a], Ian Chesser [b], Brandon Runnels [c], Nikhil Chandra Admal [a,*]

[a] Department of Mechanical Science and Engineering, University of Illinois at Urbana-Champaign, Urbana, IL, USA
[b] X Computational Physics Division, Los Alamos National Laboratory, Los Alamos, New Mexico, NM, USA
[c] Department of Aerospace Engineering, Iowa State University, Ames, IA, USA

ARTICLE INFO

Keywords:
Coupling factor
Asymmetric tilt grain boundaries
Grain boundary plasticity
Disconnections
Bicrystallography

ABSTRACT

Grain Boundaries (GB) play an important role in determining the behavior of polycrystalline materials. While the mechanisms of motion and associated shear response for symmetric tilt grain boundaries (STGBs) are well studied, the same is not true for asymmetric tilt grain boundaries (ATGBs) despite their greater prevalence in polycrystals. This study aims to investigate the shear response of a large collection of asymmetric tilt grain boundaries (ATGBs) using molecular dynamics (MD) simulations and interpret the data using a discrete disconnections model that works remarkably well for STGBs. MD simulations of shear-driven ATGBs show that the plastic shear (shear coupling factor) in the region swept by a GB exhibits a complex dependence on the inclination angle, and this dependence changes with the misorientation of the GB. In addition, the shear response was observed to be highly sensitive to the applied shear rate and temperature. Recognizing the spatial and temporal scale limitations of MD simulations, we extended the discrete disconnections mesoscale model of Khater et al. (2012) to calculate the nucleation barriers of disconnection modes and predict the effective shear coupling of an ATGB. We observed that the mesoscale model's predictions of the shear coupling factor of ATGBs do not agree with those observed in MD simulations. Finally, we examine the hypotheses of our mesoscale model that contribute to disagreements between MD simulations and the mesoscale model and propose improvements to the mesoscale model for future work.

1. Introduction

Grain boundaries (GBs) play an important role in determining the mechanical properties of polycrystalline materials. In particular, the effects of GBs are pronounced in nanocrystalline materials due to their large GB area-to-volume ratio. The use of nanocrystalline materials as catalysts [1], fuel cells [2], lithium-ion batteries [3], and materials with superior mechanical properties [4] under extreme thermomechanical conditions has spurned extensive research on understanding the mechanics of GB evolution. During high-stress deformation and elevated temperatures, GB evolution is accompanied by plastic shearing of the region swept by the GB. The coupling of plastic shear to GB motion, commonly referred to as *shear coupling*, is expressed in terms of the *coupling factor*, defined as the ratio of tangential grain translation velocity to the normal GB velocity. Shear coupling in a large number of symmetric tilt grain boundaries (STGBs) and some mixed (tilt and twist) GBs has been observed in experiments [5–8] and demonstrated using molecular dynamics (MD) simulations [9].

Studies on the shear coupling of GBs have largely been limited to STGBs. Using MD simulations of a large collection of STGBs and a few mixed GBs, Homer et al. [9] demonstrated that the coupling factors of a majority of the STGBs agree well with the predictions of the Frank–Bilby equation, wherein an STGB is interpreted as an array of lattice dislocations. However, a few exceptions were also noted. Thomas et al. [10] further explored the role of stress and boundary conditions on shear coupling. By employing boundary conditions that restrict the grain motion corresponding to shear coupling observed in an unconstrained bicrystal, it was shown that the sign of the shear coupling can be inverted. The change in the shear coupling was attributed to the change in the local stress state resulting from the boundary conditions that inhibit the shear coupling observed in an unconstrained bicrystal. The restraining boundary conditions manifest naturally in polycrystals, wherein a grain is constrained by its neighboring grains.

The occurrence of multiple shear coupling modes, depending on the local stress state, and in-situ observations [11] of GB motion have motivated the introduction of disconnections – which are interfacial line defects with a Burgers vector and a step character – as fundamental building blocks of GB plasticity. The central idea behind the

---

* Corresponding author.
E-mail address: admal@illinois.edu (N.C. Admal).

https://doi.org/10.1016/j.actamat.2024.119994
Received 4 November 2023; Received in revised form 4 May 2024; Accepted 8 May 2024
Available online 11 May 2024
1359-6454/Published by Elsevier Ltd on behalf of Acta Materialia Inc.

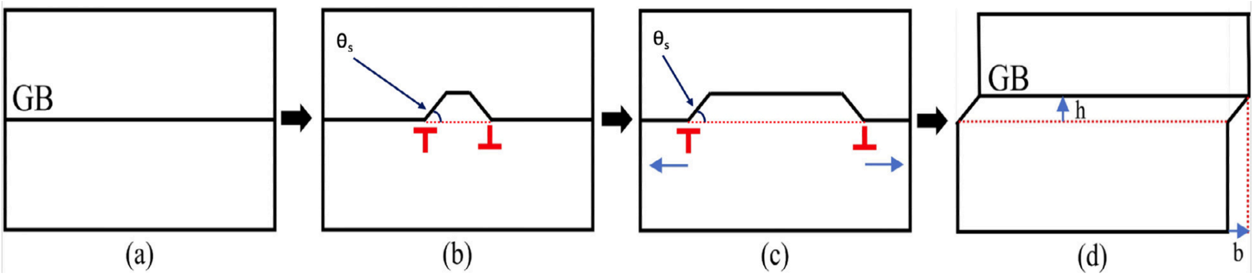

Fig. 1. A schematic depicting a disconnection-mediated GB motion. A GB (a) in a bicrystal subjected to shear migrates by nucleating a disconnection dipole (b, h) as shown in (b). (c) shows the subsequent glide of disconnections along the GB, which ultimately results in a translation of the GB by h and a plastic shear b/h of the swept region, as shown in (d). Angle created by the disconnection dipole θ_s is shown in (b) and (c).

disconnections-mediated migration of an STGB is that boundary motion is a result of nucleation and glide of disconnections along the GB. The non-unique shear coupling of GBs is attributed to the presence of multiple disconnection modes, and the propensity to nucleate a mode depends on the mode's local stress-dependent nucleation barrier. Using the disconnection nucleation model of Khater et al. [12], Han et al. [13] showed that for STGBs the shear coupling factors predicted by the disconnections model are in reasonable agreement with those observed in MD simulations of Homer et al. [9]. In particular, the dependence of shear coupling of STGBs on the nature of the driving force – shear stress vs. chemical potential – was noted.

Despite recent advances in our understanding of STGBs, the mechanisms of asymmetric tilt grain boundary (ATGB) migration remain elusive. This can be attributed to the lack of data spanning the large variety of ATGBs prevalent in polycrystals. ATGBs are known to have a significant effect on the mechanical properties of a material. For example, Singh and Parashar [14] demonstrated the effect of inclination angle on the tensile strength of Niobium and observed that the yield strength increases with the inclination angle. In addition, Lin et al. [15] reported that the presence of $\Sigma 3$ ATGBs leads to a change in the shock response of a material: the shock front of bicrystal was found to become wider than that of the monocrystal since GB plasticity was triggered when the elastic wave crossed the GB. Shock loading can also lead to migration of ATGBs [16]. The structure of the GBs remains unaffected by such loading and it is the shock-induced shear stress difference between the two sides of the GB that causes the migration [16].

Although ATGBs are more prevalent in polycrystals than their symmetric counterparts, studies such as those mentioned above are rare. Due to the lack of symmetry, ATGB properties – such as energy, mobility, and coupling factor – demonstrate large variance, and are therefore harder to quantify. Atomic scale investigations using molecular statics or dynamics simulations are also limited due to the large system size required to impose periodic boundary conditions (PBCs).[1] Most ATGB modeling efforts have focused on the determination of GB structure and energy [17–21], while investigations into their kinetic behavior [22–28] have largely been limited to a select few special ATGB cases.

The critical role of ATGBs in polycrystal plasticity and the paucity of experimental and simulation data on ATGB shear coupling motivate the first goal of this paper: *undertake an extensive survey of ATGB shear coupling using MD simulations.* In particular, we will focus on the dependence of the shear coupling factor on the inclination angle in $[0\,0\,1]$, $[1\,1\,0]$, and $[1\,1\,1]$ tilt GBs in face-centered cubic (fcc) Cu and Al under different shear rates and temperatures. While MD is a valuable tool for exploring shear coupling mechanisms, its use is restricted to extremely high shear rates compared to those imposed in experiments, which motivates our second goal: *develop a discrete disconnections-based mesoscale model for GB migration to predict shear coupling factors of GBs predict the shear coupling factors of ATGBs using the disconnection nucleation model of Khater et al. [12] adapted to ATGBs.* A key highlight of the tools employed and the ATGB migration model developed in this paper is that they are applicable to *any* crystal system and tilt axes. Smith normal form (SNF) bicrystallography [29], a framework developed by the last author to explore the bicrystallographic properties of GBs, plays a central role in our atomic and mesoscale investigations.

The paper is organized as follows. Section 2 focuses on the tools to explore ATGBs at the atomic scale and the development of a mesoscale model for GB migration. In particular, Section 2.1 describes SNF bicrystallography and its use in constructing ATGBs and enumerating their disconnection modes. Section 2.2 describes details of MD simulations, and Section 2.3 introduces the discrete disconnection model for disconnection nucleation in ATGBs. In Section 3, we present and compare the results of MD simulations and the mesoscale model. We summarize and conclude in Section 4.

Notation: In this paper, vectors are donated by lowercase letters in bold font. Lattices are denoted by uppercase letters in Calligraphic font (e.g. $\mathcal{A}$). $[l\,m\,n]_{\mathcal{A}}$ represents a vector in $\mathcal{A}$, where l, m, and n are the vector's integer coordinates. Similarly, $(p\,q\,r)_{\mathcal{A}}$ represents a lattice plane in $\mathcal{A}$ where p, q, and r are the plane's Miller indices. The subscript $\mathcal{A}$ is usually dropped if the lattice is clear from the context. An STGB with boundary plane $(p\,q\,r)$ and tilt axis $[l\,m\,n]$ is denoted by $\Sigma n[l\,m\,n](p\,q\,r)$, where n is the misorientation-dependent integer Σ-value. Similarly, an ATGB whose boundary plane has Miller indices $(p_1\,q_1\,r_1)$ and $(p_2\,q_2\,r_2)$ with respect to the two adjoining lattices is denoted by $\Sigma n[l\,m\,n](p_1\,q_1\,r_1)(p_2\,q_2\,r_2)$.

2. Methods

In this section, we describe the methods employed in this paper to investigate the shear coupling of ATGBs. We use MD to simulate shear-driven ATGB motion at the atomic scale, and at the mesoscale, we extend the discrete disconnection model of Khater et al. [12] to ATGBs. We begin our discussion with the framework of SNF bicrystallography as it plays a critical role in the implementation of the above methods.

2.1. SNF bicrystallography

A systematic survey of ATGB migration using MD simulations, and analysis of the simulations using the disconnections framework entails the enumeration of rational ATGBs – that are amenable to PBCs – and the disconnection modes they host. A disconnection $(\boldsymbol{b}, h)$ is a GB line defect with a Burgers vector $\boldsymbol{b}$ and a step height h. The nucleation of a disconnection loop in a GB and its subsequent expansion results in the translation of the GB by the step height h, and the region swept by the GB undergoes a plastic shear of magnitude equal to the coupling factor b/h. Fig. 1 shows a schematic of a glide disconnection, where the Burgers vector is parallel to the GB. A GB can host multiple

---

[1] To impose PBCs, the system size along a GB should be a multiple of the periodicity of the coincidence site lattice along the GB, which is large for most high-index ATGBs.

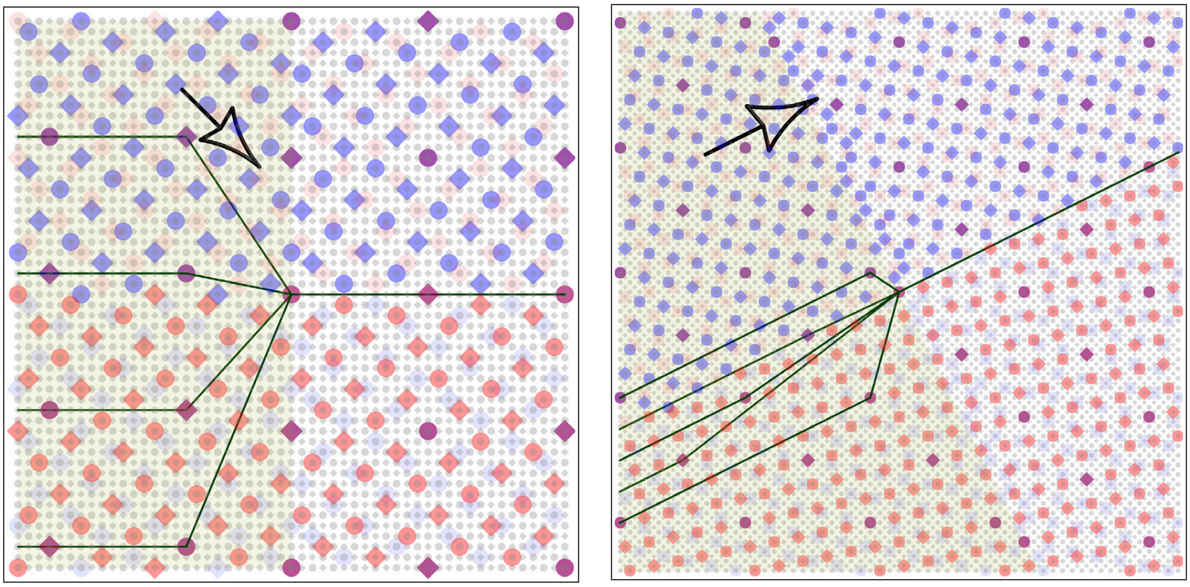

(a) A non-glide disconnection in $\Sigma 13[0\,1\,0](2\,0\,3)$ STGB   (b) A glide disconnection in $\Sigma 13[0\,1\,0](7\,0\,\bar{9})(3\,0\,\overline{11})$ ATGB

Fig. 2. The Burgers vector $\boldsymbol{b}$ of the disconnection is a DSCL vector indicated by an arrow (not to scale) in each plot.

disconnection modes that have identical Burgers vectors but differ in step heights.

SNF bicrystallography is a powerful framework based on integer matrix algebra to enumerate disconnection modes in GBs, automate the generation of rational GBs, and identify simulation domains that are amenable to PBCs. The SNF framework results in dimension-independent algorithms that apply to any crystal system and is implemented as an opensource C++ library *open Interface Lab* (`oiLAB`), accessible at https://github.com/oilab-project/oILAB.git. In what follows we will describe the essential features of SNF bicrystallography. For further details, we refer the reader to [29].

The SNF framework begins with two lattices $\mathcal{A}$ and $\mathcal{B}$ with respective structure matrices $\boldsymbol{A}$ and $\boldsymbol{B}$, where the columns of a structure matrix store the basis of its corresponding lattice. In the context of this work, lattice $\mathcal{B}$ is a rotated version of lattice $\mathcal{A}$, i.e. $\boldsymbol{B} = \boldsymbol{RA}$, where $\boldsymbol{R}(\theta)$ is a rotation matrix corresponding to a misorientation angle θ and a prescribed tilt axis. Moreover, the misorientation angle belongs to a collection of discrete angles that result in a 3D *coincident site lattice* $\mathcal{C} := \mathcal{A} \cap \mathcal{B}$. A key step in SNF bicrystallography is the transformation of basis vectors of lattices such that the new basis vectors of the lattices, collected in structure matrices $\boldsymbol{A}^{\parallel}$, $\boldsymbol{B}^{\parallel}$, and $\boldsymbol{C}^{\parallel}$, are parallel. This transformation makes it straightforward to introduce a fourth lattice $\mathcal{D}$, called the *displacement shift complete lattice* (DSCL), defined as the smallest lattice that contains $\mathcal{A}$ and $\mathcal{B}$, and therefore $\mathcal{C}$ as well.[2] The parallel basis vectors yield mappings between the four lattices and their respective reciprocal lattices, enabling us to construct numerous ATGBs using lattice-agnostic algorithms based on integer algebra.

In addition, the parallel basis vectors play a central role in the proof of Theorem 1, which characterizes the translational invariance of a GB and ultimately leads to the definition of a disconnection.

Theorem 1 (*Admal et al.* [29]). *Translating lattice $\mathcal{A}$ by a vector $\boldsymbol{b} \in \mathcal{D}$ with $\mathcal{B}$ fixed results in a shift $\lambda_{\mathcal{A}} \in \mathcal{B}$ of the CSL. In other words*

$$(\mathcal{A} + \boldsymbol{b}) \cap \mathcal{B} = \mathcal{C} + \lambda_{\mathcal{A}}.$$

Fig. 2 conveys the essence of Theorem 1 — translating the shaded region (top left) of the blue lattice by a DSCL vector $\boldsymbol{b}$ (shown in arrows, but not to scale) results in a CSL shift $\lambda_{\mathcal{A}}$. Moreover, the translation disrupts one-half of the GB structure. To preserve its structure, the GB migrates in its normal direction $\boldsymbol{n}_{\mathcal{A}}$ by a distance $h_{\mathcal{A}} = \lambda_{\mathcal{A}} \cdot \boldsymbol{n}_{\mathcal{A}} + nH$, where n is an integer and H is the CSL lattice plane spacing along $\boldsymbol{n}_{\mathcal{A}}$, resulting in a dislocation $\boldsymbol{b}$ and a GB step of height h at the center of the domain. The collection of all $(\boldsymbol{b}, h_{\mathcal{A}})$ pairs represents the disconnection modes of the GB. To summarize, given two lattices $\mathcal{A}$ and $\mathcal{B}$ that share a CSL, SNF bicrystallography can be used to construct arbitrary rational GBs and enumerate their disconnection modes.

Table 1
This study included 244 ATGBs distributed over 3 tilt axes and 7 misorientation angles.

Tilt axis	Element	Sigma number (misorientation)	#ϕ simulated
[0 0 1]	Cu	$\Sigma 5$ (36.86°)	38
		$\Sigma 13$ (22.62°)	25
		$\Sigma 25$ (16.26°)	23
[1 1 1]	Cu	$\Sigma 21$ (21.78°)	23
		$\Sigma 7$ (38.21°)	26
[1 1 0]	Al	$\Sigma 9$ (38.94°)	57
		$\Sigma 11$ (50.47°)	52

The generality of SNF bicrystallography enables us to enumerate not only glissile disconnections (Fig. 2(b)) but also sessile disconnections that have a climb component in their Burgers vector (Fig. 2(a)). Glissile and sessile disconnections mediate GB motion, however, the migration of the latter along the GB is a result of GB diffusion. In Section 2.3, we introduce a mesoscale model to analyze the energetics of disconnections enumerated by SNF bicrystallography and ultimately predict the shear coupling factors of ATGBs.

2.2. Atomistic simulations of shear coupling in ATGBs

In this section, we introduce the simulated GBs and outline the details of MD simulations for ATGBs with three tilt axes, ([0 0 1], [1 1 0], [1 1 1]), and two species (Cu, Al), modeled using EAM potentials [30, 31]. From a list of ATGBs identified by SNF bicrystallography, the simulated GBs were selected such that the sizes of the period vectors are at most 50 times the lattice spacing. Table 1 lists the tilt axes, misorientation angles, and the number of inclination angles investigated in this study.

The MD simulations were performed using LAMMPS [32]. Each bicrystal was constructed by rotating two grains about the tilt axis

---

[2] $\mathcal{D}$ is a fictitious lattice as some of its points are unoccupied.

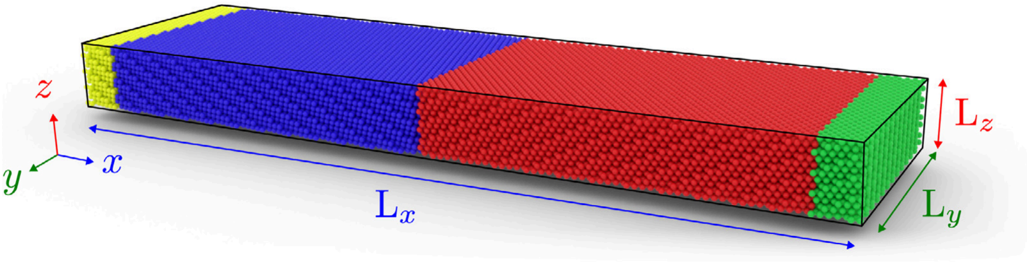

Fig. 3. A bicrystal with an ATGB, visualized using OVITO [33]. Blue and red colored atoms represent the two grains of the bicrystal. The atoms in the top and bottom layers of the simulation box, colored yellow and green, are used to impose a strain rate. The bicrystal is oriented such that the GB is parallel to the yz-plane and the tilt axis is along the z-axis. PBCs are imposed along the y and z directions. (For interpretation of the references to color in this figure legend, the reader is referred to the web version of this article.)

by the misorientation angle, and the GB was identified using the inclination angle. The bicrystals were oriented such that the tilt axis is along the z-axis, the GB plane lies in the $y-z$ plane, and the GB normal is along the x-axis. PBCs were imposed in the y and z directions. The dimension of the simulation cell along the x-axis was $L_x = 30\,\mathrm{nm}$, and the dimensions L_y and L_z along the y and z directions, respectively, were set equal to integer multiples of two CSL vectors along the y and z-axes. The inclination angles were selected such that $10\,\mathrm{nm} \leq L_y \leq 40\,\mathrm{nm}$ and $1.5\,\mathrm{nm} \leq L_z \leq 2.5\,\mathrm{nm}$ (based on the tilt axis) for all simulations. The simulation box sizes in the current study are larger than those in previous studies. For example, the box dimensions along the period vectors of the GBs are twice those considered in Trautt et al. [23].

A block of atoms at the top and the bottom of the bicrystal (highlighted in yellow and green respectively in Fig. 3) were fixed to act as boundary layers in the non-periodic direction. The thickness of these blocks was larger than the cutoff radii of the interatomic potentials used for Cu and Al. To subject the system to a constant shear rate the atoms in the top layer are translated at a constant velocity dictated by the imposed strain rate. We examined multiple strain rates until the bicrystal undergoes a 20% strain. Due to the time scale limitation of MD simulations, the strain rates are much higher than the laboratory-scale strain rates. To infer shear coupling factors at lower strain rates that are inaccessible to MD simulations, we examined the convergence of coupling factors as the strain rate was decreased three orders of magnitude from $10^8\,\mathrm{s}^{-1}$ to $10^6\,\mathrm{s}^{-1}$.

Beginning with the coherent dichromatic pattern, we used the conjugate gradient method to minimize the energy of the bicrystal. Subsequently, an NPT ensemble is simulated using the Nosé–Hoover thermostat with a temperature of $600\,\mathrm{K}$ or $900\,\mathrm{K}$ and a pressure of 1 atmosphere. We explicitly controlled σ_{yy} and σ_{zz} and set them to 1 atm. Consequently, we did not control the lengths L_y and L_z of the box. We did not explore the role of individual microstates as our goal, motivated by STGBs, was to investigate the trends in shear coupling that can be attributed entirely to disconnections as opposed to microstates. The GBs were equilibrated for $1\,\mathrm{ns}$ before imposing a strain rate. During the straining phase – and in particular at high strain rates – we observed that some ATGBs do not remain flat as they migrate and show a variable coupling factor across their length. Fig. 4 shows two initially flat $\Sigma5[0\,0\,1](\overline{14}\,13\,0)(\overline{19}\,2\,0)$ and $\Sigma5[0\,0\,1](\bar{4}\,13\,0)(\overline{11}\,8\,0)$ ATGBs (a and d) migrating and bowing during the straining phase (b and e). Notably, we found that if the system was allowed to equilibrate after the straining phase, the GB obtains an equilibrium shape (c and f). Moreover, we observed that the bowing decreased for lower strain rates suggesting that under experimental strain rates, ATGBs will migrate without bowing. Therefore, we chose to equilibrate the bicrystal after the straining phase, with the atoms in the two boundary layers fixed, for the GB to flatten. During this equilibration phase, the coupling factor was recorded at multiple points (fiducial markers in Fig. 4) along the GB every $0.2\,\mathrm{ns}$ followed by a spatial averaging to obtain the effective coupling factor at each timestep. This is a notable departure from previous studies [23–25], which recorded coupling factors during the straining phase.

2.3. Extended Khater model to predict shear coupling factors of ATGBs

The differences in the length and time scales of MD simulations and experiments motivate the development of a mesoscale model for GB motion to predict shear coupling in ATGBs. Moreover, the scale limitations of MD are more pronounced in ATGBs – compared to STGBs – as many have large period vectors and their shear coupling is relatively more sensitive to strain rates, requiring larger simulation domains and longer simulation times. Inspired by recent experiments and MD simulations [11,34,35] that support the hypothesis that disconnections are the primary carriers of GB plasticity, we make use of model proposed by Khater et al. [12], based on the disconnections-based description of GB motion.

Recall from Section 2 that disconnection modes originate from bicrystallography and a GB can host multiple disconnection modes. Thomas et al. [10],Chen et al. [36] reasoned that the multiplicity of disconnection modes renders the GB mobility and the shear coupling factor as properties non-intrinsic to the GB due to their dependence on the local stress state. More generally, a kinetic property can be interpreted as a weighted average of the corresponding property of individual disconnection modes, where the weight associated with a mode depends on its configurational force-dependent nucleation barrier. Therefore, in what follows, we focus our attention on predicting the nucleation barriers of individual disconnection modes by extending the discrete disconnection model of Khater et al. [12]. Subsequently, we use the nucleation barriers to compute the expected values of the shear coupling factors of GBs.

To describe our mesoscale model, we begin with the following four assumptions:

(A1) A GB is a perfectly flat interface and continues to remain flat as it migrates.
(A2) Disconnection with the smallest nucleation barrier mediates the shear coupling of a GB. We assume that the nucleation of disconnections is homogeneous.
(A3) The grains adjoining a GB are elastically isotropic.
(A4) Shear coupling of GBs is a consequence of *effective* glide of disconnections along a GB.

Assumptions (A1), (A2), and (A3) are inherited from the model's predecessor [12], used by Han et al. [13] to calculate the coupling factors of STGBs in Cu. While MD simulations of STGBs demonstrate that the flatness assumption in (A1) holds for most STGBs, the same is not true for ATGBs due to the curving of the GB, as noted in Section 2.2. However, since the curving decreases with the strain rate, we assert that the flatness assumption is reasonable at the low strain rates of experiments. While Assumption (A2) remains to be investigated for ATGBs, the observation that ATGBs that slip under shear stress (infinite coupling factor) host disconnections with zero step height (see Fig. 2(b)) lends credence to its validity. The notion of effective glide in Assumption (A4) will be made precise towards the end of this section.

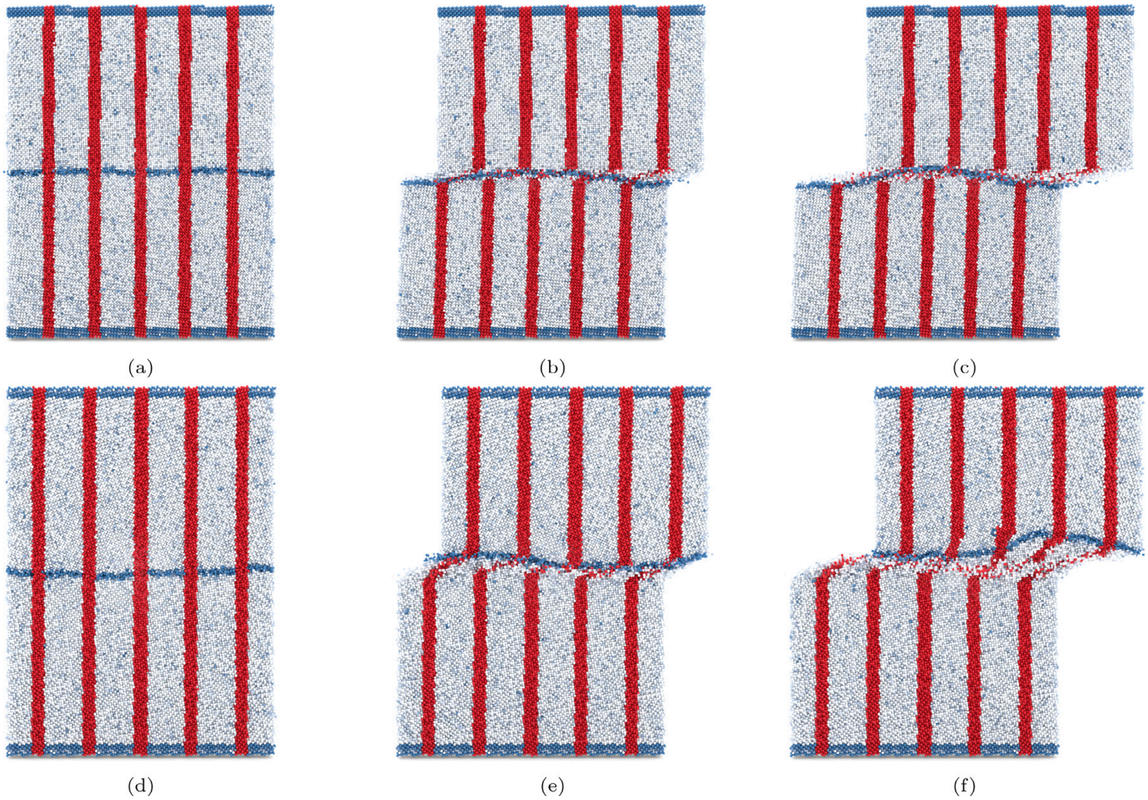

Fig. 4. Shear coupling in $\Sigma5[0\,0\,1](\overline{14}\,13\,0)(\overline{19}\,2\,0)$ (a, b, c) and $\Sigma5[0\,0\,1](\bar{4}\,13\,0)(\overline{11}\,8\,0)$ (d, e, f). ATGB migration is conveyed by the magenta-colored fiducial markers. The centrosymmetry parameter in OVITO was used to identify the GBs. The initially flat GBs in (a) and (d) curve as they migrate during the straining phase (b,e). During subsequent equilibration for 10 ns, the GBs flatten (c, f). Multiple fiducial markers (highlighted in red) are used to calculate the coupling factor at different points along the GB. Average of these coupling factors is reported as the effective coupling factor for the GB at each timestep. (For interpretation of the references to color in this figure legend, the reader is referred to the web version of this article.)

The discrete disconnection model of Khater et al. [12] assumes that the energy per unit length of a disconnection dipole formed by disconnections $(\boldsymbol{b}, h)$ and $(-\boldsymbol{b}, h)$ is of the form

$$E(\boldsymbol{b}, h) = 2E_{\text{step}} + 2E_{\text{core}} + E_{\text{int}} + W, \tag{1}$$

where E_{step} is the step energy, E_{core} is the disconnection core energy, E_{int} is the elastic interaction energy, and W is the work done by external force. The step energy is assumed to be a linear function of h:

$$E_{\text{step}} = \Gamma_s h, \text{ where } \Gamma_s = \frac{\gamma_s - \gamma cos\theta_s}{sin\theta_s}, \tag{2}$$

γ_s is the energy density (per unit area) of the step, γ is the energy density of the flat region of the GB, and θ_s is the angle of the step (see Fig. 1).

The sum of the interaction and core energies of a disconnection dipole is given by

$$2E_{\text{core}} + E_{\text{int}} = 2\kappa b^2 \log\frac{\delta}{\delta_0}, \text{ where } \kappa = \frac{\mu}{4\pi(1-\nu)}, \tag{3}$$

μ is the shear modulus, ν is the Poisson's ratio, δ is the separation between the two opposite disconnections, and δ_0 is the effective core size of the disconnections. The work done by the external force depends on the nature of the force. For example, if the system is driven by an external stress τ, $W = -\tau b\delta$, and if it is driven by a chemical potential ψ, $W = -\psi h\delta$. Therefore, the total energy per unit length of a disconnection dipole is given by

$$E(\boldsymbol{b}, h) = \begin{cases} 2\Gamma_s|h| + 2\kappa b^2 \log\frac{\delta}{\delta_0} - \tau b\delta & \text{if shear stress } \tau\text{-driven,} \\ 2\Gamma_s|h| + 2\kappa b^2 \log\frac{\delta}{\delta_0} - \psi h\delta & \text{if chemical potential } \psi\text{-driven.} \end{cases} \tag{4}$$

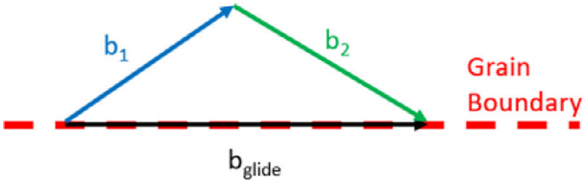

Fig. 5. Shear coupling factor of a GB is set equal to the coupling factor of the glide disconnection mode $(\boldsymbol{b}, h)$ with the smallest nucleation barrier. The model assumes the mechanisms for nucleating $(\boldsymbol{b}, h)$ include climb disconnections $(\boldsymbol{b}_1, h_1)$ and $(\boldsymbol{b}_2, h_2)$ such that $\boldsymbol{b}_1 + \boldsymbol{b}_2 = \boldsymbol{b}$ and $h_1 + h_2 = h$, resulting in a climb-mediated effective glide.

The energy in the above two cases is $-\infty$ at $\delta = 0$, and reaches a maximum at a critical $\delta = \delta^*$ at which $dE/d\delta = 0$, and decreases thereafter. The critical separation δ^* is given by

$$\delta^* = \begin{cases} \frac{2\kappa b^2}{\tau b} & \text{if shear force } \tau\text{-driven,} \\ \frac{2\kappa b^2}{\psi h} & \text{if chemical potential } \psi\text{-driven.} \end{cases} \tag{5}$$

The nucleation barrier for the disconnection dipole is the energy evaluated at δ^*. Substituting (5) in (4), we obtain the nucleation barrier

$$E^*(\boldsymbol{b}, h) = \begin{cases} 2\Gamma_s|h| + 2\kappa b^2 \log\frac{2\kappa b^2}{e\tau b\delta_0} & \text{if shear force } \tau\text{-driven,} \\ 2\Gamma_s|h| + 2\kappa b^2 \log\frac{2\kappa b^2}{e\psi h\delta_0} & \text{if chemical potential } \psi\text{-driven.} \end{cases} \tag{6}$$

Invoking Assumption (A4), Han et al. [13] spanned all glide disconnection modes of an STGB in Cu and predicted its shear coupling factor

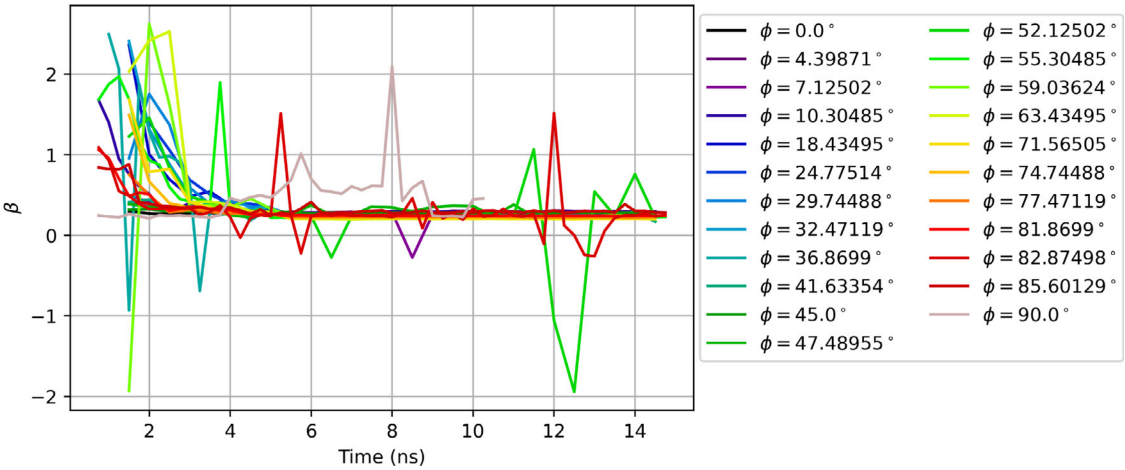

Fig. 6. The variation of coupling factor with respect to time in $\Sigma 25[001]$ ATGBs. A strain rate of $10^6\,\mathrm{s}^{-1}$ was applied for the first 5 ns of the simulation and subsequently the boundary was allowed to equilibrate.

as the coupling factor of the glide disconnection with the smallest nucleation barrier. In what follows, we extend the study of Han et al. [13] to ATGBs. Since the Burgers vectors of glide disconnections in ATGBs are typically orders of magnitude larger than the lattice constant, their nucleation barriers predicted by (6) are far higher than those of non-glide disconnections. Since an effective disconnection glide $(\boldsymbol{b}, h)$ can be realized by reactions involving non-glide disconnections $(\boldsymbol{b}_1, h_1)$ and $(\boldsymbol{b}_2, h_2)$ such that $\boldsymbol{b}_1 + \boldsymbol{b}_2 = \boldsymbol{b}$ and $h_1 + h_2 = h$ (see Fig. 5), we postulate that ATGB migration is mediated by such reactions. The nucleation barrier associated with this reaction can be calculated assuming an Arrhenius-type process. The time taken for each of these processes to take place is:

$$t_1 = \nu^{-1}\exp\left(\frac{E^*(\boldsymbol{b}_1, h_1)}{k_B T}\right), \qquad t_2 = \nu^{-1}\exp\left(\frac{E^*(\boldsymbol{b}_2, h_2)}{k_B T}\right), \tag{7}$$

where ν is the attempt frequency, k_B is the Boltzmann constant, and T denotes temperature. $E^*(\boldsymbol{b}_1, h_1)$ and $E^*(\boldsymbol{b}_2, h_2)$ denote the nucleation energies of the two non-glide disconnections. The total time required for the reaction can then be used to arrive at an effective energy associated with the reaction (assuming attempt frequency to be 1 throughout), given as:

$$E^*_{\text{climb assisted}}(\boldsymbol{b}, h) = k_B T \log\left(\exp\left(\frac{E^*(\boldsymbol{b}_1, h_1)}{k_B T}\right) + \exp\left(\frac{E^*(\boldsymbol{b}_1, h_1)}{k_B T}\right)\right). \tag{8}$$

Clearly, $E^*_{\text{climb assisted}}(\boldsymbol{b}, h)$ can be less than or equal to the nucleation barrier $E^*(\boldsymbol{b}, h)$ of the pure glide disconnection. Therefore, we postulate that the nucleation barrier of disconnection glide $(\boldsymbol{b}, h)$ is given by the following minimization over all (glide and non-glide) disconnection modes that can mediate an effective glide:

$$\overline{E}(\boldsymbol{b}, h) = \min_{\substack{\boldsymbol{b}_1, \boldsymbol{b}_2 \in D: \\ \boldsymbol{b}_1 + \boldsymbol{b}_2 = \boldsymbol{b}}} k_B T \log\left(\exp\left(\frac{E^*(\boldsymbol{b}_1, h_1)}{k_B T}\right) + \exp\left(\frac{E^*(\boldsymbol{b}_1, h_1)}{k_B T}\right)\right). \tag{9}$$

Revisiting the STGBs studied by Han et al. [13] using (9), we noted that the minimizer in (9) for STGBs is typically the trivial solution $\boldsymbol{b}_1 = \boldsymbol{b}$ and $\boldsymbol{b}_2 = \boldsymbol{0}$. In other words, (9) confirms that the strategy of Han et al. [13] to ignore non-glide disconnections is energetically consistent. However, in the case of ATGBs, the solution to (9) is invariably non-trivial, and therefore we conclude that disconnection glide is climb-mediated. The climb processes involving bulk vacancy diffusion will be inaccessible on MD timescales. However, GB diffusion-mediated climb or stress-driven GB core-mediated climb processes are possible.

To compute the coupling factor of an ATGB, we first enumerate all its disconnection modes using SNF bicrystallography. The nucleation barrier of each glide disconnection – possibly mediated by climb – is computed using Eq. (9), and the coupling factor is set equal to that of the glide disconnection mode with the smallest barrier. In Section 3, we implement the mesoscale model and compare its predictions to MD simulations described in Section 3.2. The material parameters of Cu used for the nucleation barrier calculations are $\mu = 44\,\mathrm{GPa}$, $\nu = 0.3$, $\theta_s = \pi/2\,\mathrm{rad}$, $\delta_0 = b_i/\alpha$, and $\alpha = 3$ while for Al are $\mu = 24\,\mathrm{GPa}$, $\nu = 0.33$, $\theta_s = \pi/2\,\mathrm{rad}$, $\delta_0 = b_i/\alpha$, $\alpha = 3$, and $T = 600\,\mathrm{K}$. The inclination dependent GB energy (γ_s) for $\Sigma 5[001]$, $\Sigma 13[001]$, $\Sigma 9[110]$ and $\Sigma 11[110]$ were derived based on the calculations done by Tschopp et al. [37]. For the other GBs in this study we used γ_s equal to the STGB energy, due to lack of data.

3. Results

In this section, we present the shear coupling factors of ATGBs in Cu and Al bicrystals predicted by atomistic simulations and the discrete disconnection model. The inclination angles of ATGBs discussed in this section span 0° to 90° for each of the misorientations listed in Table 1. The ranges of the shear coupling factor versus inclination angle plots (Figs. 9 to 15) presented in this section omit the large shear coupling factors corresponding to GB sliding. The plots in the Supplementary cover the entire data range. In addition, MD simulation data presented in this section is shared in the Mendeley dataset repository [38].

3.1. Atomistic simulations

Figs. 9 to 11 show plots of coupling factors of $\Sigma 5$, $\Sigma 25$, and $\Sigma 13$-[001] ATGBs for various shear rates and temperatures. Figs. 14 and 15 show coupling factors of $\Sigma 9$ and $\Sigma 11$-[110] ATGBs, and Figs. 12 and 13 correspond to $\Sigma 7$ and $\Sigma 21$-[111] ATGBs, respectively. The dashed line in all the plots indicates the coupling factor of the STGB. The colors in the scatter plots indicate different shear rates, and the green line plots in Figs. 9 and 10 correspond to the MD simulation results of Trautt et al. [23]. Recall from Section 3.1 that we measure coupling factors at multiple points along the GB as it migrates. At each time step (recorded every 0.2 ns) the coupling factor is spatially averaged across the GB and recorded. In the coupling factor plots, the multiple points of identical color appearing on a vertical line – corresponding to a particular shear rate and an inclination angle – refer to the spatially averaged coupling factor recorded at different time instances. The medians of these points for each inclination angle are used to draw the dark red, red, and orange line plots, corresponding to different shear rates. The clustering of the points suggests that the GB coupling factor converges with time, and variability shows that the initial coupling factors differ from the

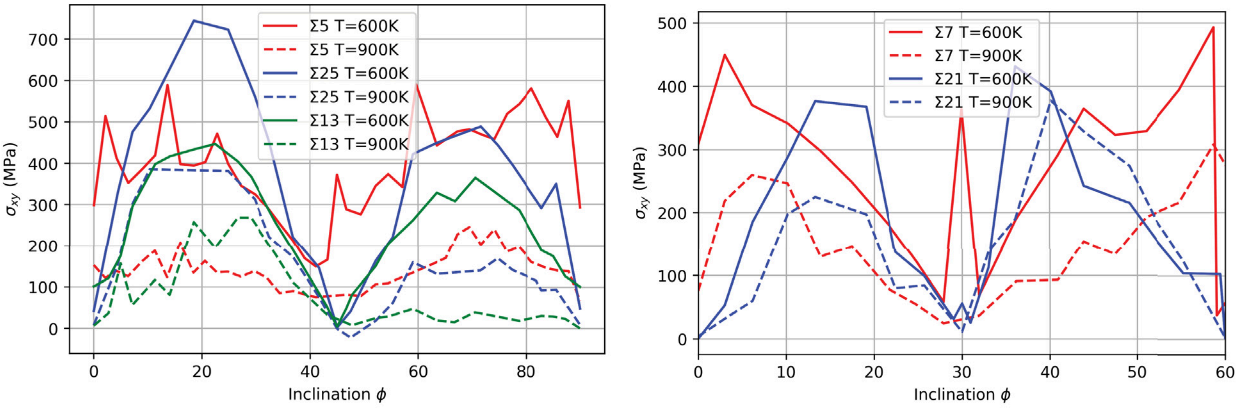

(a) Axis [001], STGBs are at 0°,45° and 90°.

(b) Axis [111], STGBs are at 0°,30° and 60°.

Fig. 7. Flow stresses for ATGBs in Cu.

steady state value. Fig. 6 shows the convergence of coupling factors with respect to time in $\Sigma 25[001]$ ATGBs at 600 K under a strain rate of $10^6\mathrm{s}^{-1}$. Similar plots for the remaining grain boundaries investigated in this paper are shown in Figures 6–11 of the Supplementary.

Flow stresses observed in ATGBs

We calculated the flow stresses for the set of simulations with the lowest strain rate ($\dot{\gamma} = 10^6\mathrm{s}^{-1}$) for each of the ATGBs investigated in this study. These stresses are plotted in Figs. 7(a), 7(b) and 8 for each of the axes considered in this study. As a direct comparison, we used the stress data provided by Trautt et al. [23] in their study of $\Sigma 25[001]$ ATGBs in Cu and Al. The flow stresses observed in this study match well with the stresses reported by them for $\Sigma 25[001]$. We did not capture the data at a rate high enough to accurately observe the peaks of stresses observed in the stick–slip type motion of the GBs, making comparison to previously calculated critical stresses infeasible. Therefore, we were not able to ascertain the assumption about homogeneous nucleation. The flow stresses show a clear trend with inclination angle of the ATGB, with stresses increasing as the ATGB moves away from STGB configuration. The stresses also show asymmetry w.r.t inclination angle that lead to similar GB structures (45° for [001], 30° for [111], 90° for [110]), similar to previously reported stresses [23]. The magnitude of stresses is observed to decrease in magnitude as the temperature increases in line with the observations made in previous studies [23].

Across all the investigated ATGBs, we observe the following trends for coupling factors:

- The coupling factors were observed to be sensitive to misorientation and inclination angles. Compared to the piecewise linear variation of STGB coupling factors with misorientation angles, as noted by Han et al. [13], the variation with respect to the inclination angle is highly nonlinear with no consistent trend across different misorientation angles. Han et al. [13] arrived at a geometry-based estimate of the coupling factor for ATGBs. However, agreement between their estimate and MD data is rather limited except for some inclinations in $\Sigma 21[111]$ and $\Sigma 5[001]$ GBs.
- The spatial variability in the coupling factor, for a given inclination and temperature, increases as the strain rate increases. A similar trend holds with respect to temperature for a given inclination and strain rate. The increase in scatter at high temperatures and strain rates is due to the highly disordered motion of a GB, as noted by Fensin et al. [24].

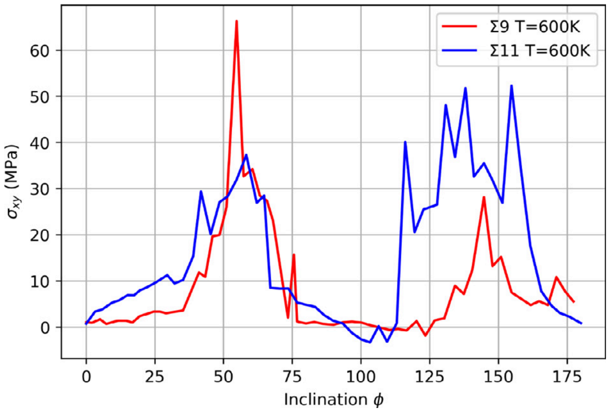

Fig. 8. Flow stresses for [110] axis ATGBs in Al, STGBs are at 0°, 90° and 180°.

- With an increase in strain rates, the scatter in coupling factors observed in the equilibration phase also increases (see Fig. 10) This is because at higher strain rates ATGB motion is interspersed by instances where sliding occurs. This leads to some parts of the GB moving to a lesser extent in the normal direction compared to others, resulting in curvature in the ATGB.
- The spread in the coupling factors for an inclination angle correlates with the curvature of the GB during its migration (see Fig. 4 for examples). As the GB equilibriates and flattens, the coupling factor converges. This can be observed in Fig. 6. Strain was applied for the first 5 ns and then the GB was allowed to equilibrate for 10 ns. The coupling factors of most ATGBs converge during the equilibration phase.
- The magnitude of the coupling factor of an ATGB increases with temperature and shear rates with a few exceptions. This can be observed by comparing Figs. 11(a) and 11(b) for $\Sigma 13[001]$, Figs. 10(a) and 10(b) for $\Sigma 25[001]$, and Figs. 12(a) and 12(b) for $\Sigma 7[111]$. We note an exception while comparing Figs. 13(a) and 13(b) for $\Sigma 21[111]$, where the magnitude of the coupling factor decreases for most inclinations at the higher temperature.
- The coupling factors of ATGBs increase with temperature in the low-to-intermediate (homogolous temperature, $T_H < 0.8$) range, with a few exceptions. While Homer et al. [9] noted a similar

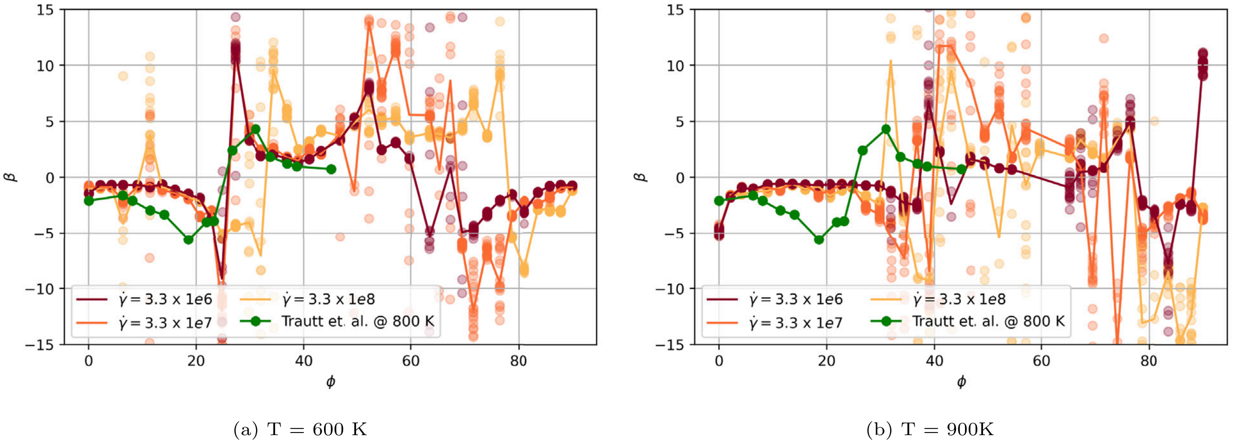

(a) T = 600 K (b) T = 900K

Fig. 9. Coupling factors for $\Sigma5[001]$ GBs for three shear rates, shown in dark red, red, and orange. The scattered points represent the spatially averaged coupling factor recorded at various times as the GB equilibrates after undergoing shear coupling. The dark red, red, and orange line plots are plotted using the median of the scattered data. The dashed line represents the coupling factor of STGB $\Sigma5(2\,1\,0)$ at 0° and 90° inclination angles. The green line plot is based on the data from Trautt et al. [23]. (For interpretation of the references to color in this figure legend, the reader is referred to the web version of this article.)

trend for STGBs, they also observed that the coupling factors of STGBs stay nearly constant at intermediate temperatures.

Next, we discuss each of the Σ boundaries separately and identify features specific to them in the following paragraphs.

$\Sigma5[0\,0\,1]$ *ATGBs*

Figs. 9(a) and 9(b) show variation of coupling factors for various strain rates, measured at 600 K ($T_H = 0.45$) and 900 K ($T_H = 0.66$), respectively. The inclination angles 0° and 90° correspond to the STGB $\Sigma5[0\,0\,1](2\,1\,0)$, and the one at 45° inclination angle is the $\Sigma5[0\,0\,1](3\,1\,0)$ STGB. From the above plots, we note that as an ATGB deviates from an STGB (0° and 90° inclination angles), the coupling factor changes sign from negative to positive. The transition in the sign of the coupling factor occurs at inclination angles ≈ 20° and 60°. This observation is consistent with the coupling factors measured at 500 K and 800 K by Trautt et al. [23] and shown in green.[3] In addition, we note from Fig. 9 that the inclination angles at which the coupling factor changes sign shifted to the right as the temperature was increased from 600 K to 900 K. However, we note that although the GB structure is symmetric with respect to the 45° inclination angle, its shear coupling response is not — the plots in Figs. 9(a) and 9(b) are not symmetric with respect to the 45° angle. Such asymmetry was also observed by Trautt et al. [23], when they considered the inclination range of −45° to 45°. We attribute this asymmetry to the difference in microstates that ATGBs attains. In addition, the spread in the coupling factor is minimal for ATGBs close to STGBs.

$\Sigma25[0\,0\,1]$ *ATGBs*

Fig. 10 shows coupling factors of $\Sigma25[0\,0\,1]$ ATGBs. The 0° and 90° inclination angles correspond to the $\Sigma25[0\,0\,1](7\,1\,0)$ STGB, and the one at 45° inclination angle is the $\Sigma25[0\,0\,1](4\,3\,0)$ STGB. Comparing Figs. 10(a) and 10(b) to Figs. 9(a) and 9(b), we note that ATGB coupling factors and their deviation from the STGB coupling factor are lower in the $\Sigma25[001]$ case. Fig. 10 also shows that our measurements – except for a few exceptions – are consistent with those of [23], obtained at 500 K and 1200 K. Exceptions to the earlier noted trend of decreasing coupling factor with increasing temperature can be observed in Fig. 10 — inclinations between 30° and 50° show higher coupling factors at 900 K compared to at 600 K, which exemplifies the high variability in ATGB migration mechanisms.

$\Sigma13[0\,0\,1]$ *ATGBs*

Behavior of $\Sigma13[0\,0\,1]$ ATGBs were observed to be similar to that of $\Sigma25[0\,0\,1]$ ATGBs in the sense that the coupling factor remains close to the STGB coupling factor at 0 K and low shear rates, as shown in Figs. 11(a) and 11(b) for 600 K and 900 K, respectively. The inclination angles 0° and 90° correspond to the STGB $\Sigma13[0\,0\,1](5\,1\,0)$, and the one at 45° inclination angle is the $\Sigma13[0\,0\,1](2\,3\,0)$ STGB. The coupling factor was observed to increase as the strain rate applied on the bicrystal is increased. However for these ATGBs, this trend was only observed for small inclination angles ($0° < \phi < 45°$) at both the temperatures. Higher inclination angle GB coupling factor did not show any appreciable change in coupling as the shear rates increased. An increase in temperature can also lead to a change in the nature of coupling, as can be seen by comparing Figs. 11(a) and 11(b). Some inclination angles shear with a negative coupling factor at 900 K, which is not observed for 600 K. The influence of the shear rate is much more pronounced in $\Sigma5[0\,0\,1]$ ATGBs, while $\Sigma13[0\,0\,1]$ ATGBs show the least sensitivity to the applied shear rate at lower temperatures.

[111] *ATGBs*

We will now discuss the simulation results of $\Sigma7[1\,1\,1]$ and $\Sigma21[1\,1\,1]$ ATGBs. Figs. 12 and 13 show plots of the coupling factor for $\Sigma7$ and $\Sigma21$ cases, respectively. The dependence of the coupling factor on the inclination angle was observed to be consistent (across varying shear rates and temperatures) for [1 1 1] tilt boundaries. Similar to the previous cases, this dependence depends on the misorientation of the GB. GB sliding was observed for a few inclination angles, and the number of such boundaries is far less compared to those in other tilt boundaries explored in this study. Due to lattice symmetry, the coupling factor was observed to be reasonably symmetric about the 30° inclination. Among the simulated GBs, we have 3 STGBs at inclination angles 0°, 30°, and 60° (see captions to Figs. 12 and 13).

As observed in previous cases, an increase in the shear rate results in a larger scatter in the coupling factor. However, Figs. 12 and 13 show that the sensitivity of the coupling factors to the shear rate was restricted to a narrow inclination angle range — close to 10° and 50° inclination angles for the $\Sigma7[1\,1\,1]$ ATGBs, and 20°–40° inclination angles for $\Sigma21[1\,1\,1]$ ATGBs. Moreover, in the $\Sigma7[1\,1\,1]$ ATGBs, the local minima in the coupling factor observed around 10° and 50° angles shift to the right as the shear rate increases. Furthermore, the $\Sigma7[1\,1\,1]$ ATGBs in the neighborhood of the 30° STGB were observed to have a

---

[3] The coupling factors reported by Trautt et al. [23] were measured at a strain rate of $10^7 s^{-1}$.

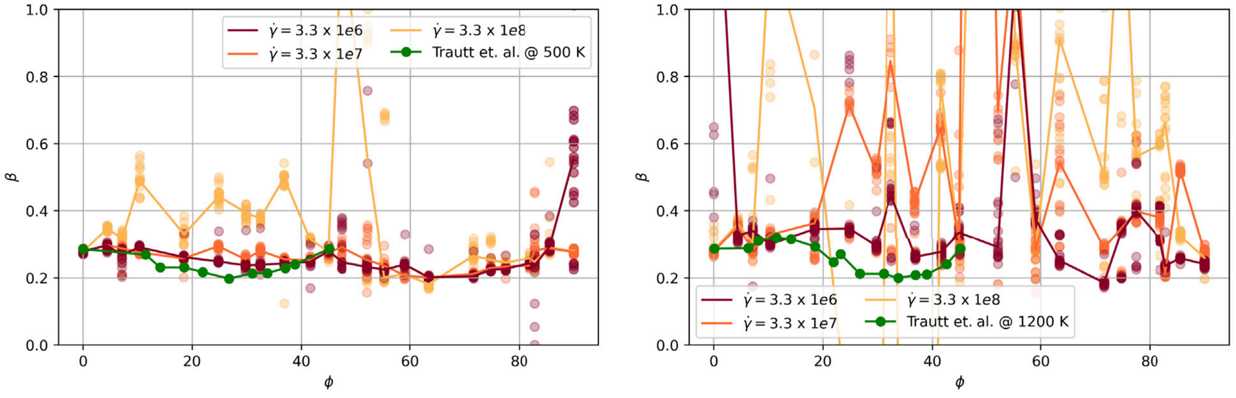

(a) T = 600 K

(b) T=900K

Fig. 10. Coupling factors for $\Sigma 25[0\,0\,1]$ GBs for different shear rates. See caption to Fig. 9, which describes the relationship between the scattered data and the line plots. The 0° and 90° inclination angles correspond to the $\Sigma 25[0\,0\,1](7\,1\,0)$ ATGB, and the one at 45° inclination angle is the $\Sigma 25[0\,0\,1](4\,3\,0)$ STGB.

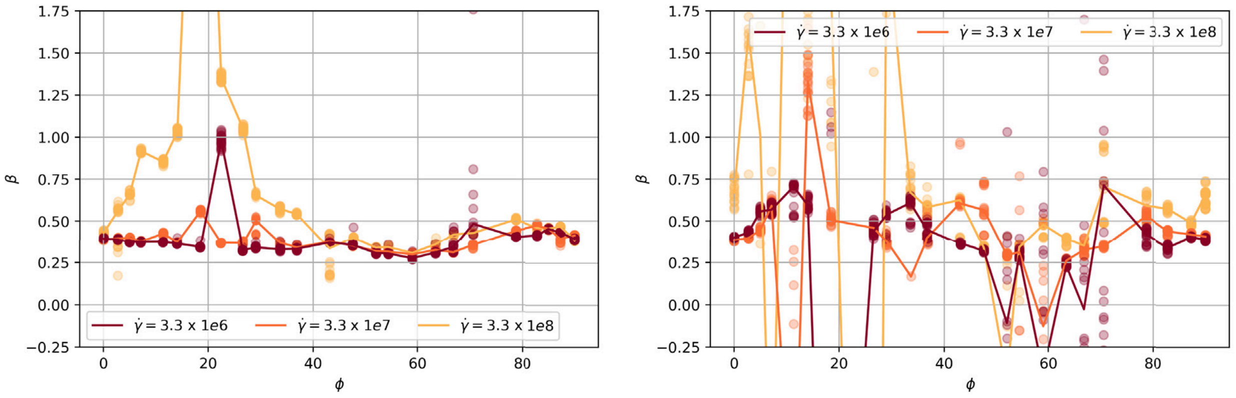

(a) T = 600 K

(b) T=900K

Fig. 11. Coupling factors for $\Sigma 13[0\,0\,1]$ GBs for different shear rates. See caption to Fig. 9, which describes the relationship between the scattered data and the line plots. The inclination angles 0° and 90° correspond to the STGB $\Sigma 13[0\,0\,1](5\,1\,0)$, and the one at 45° inclination angle is the $\Sigma 13[0\,0\,1](2\,3\,0)$ STGB.

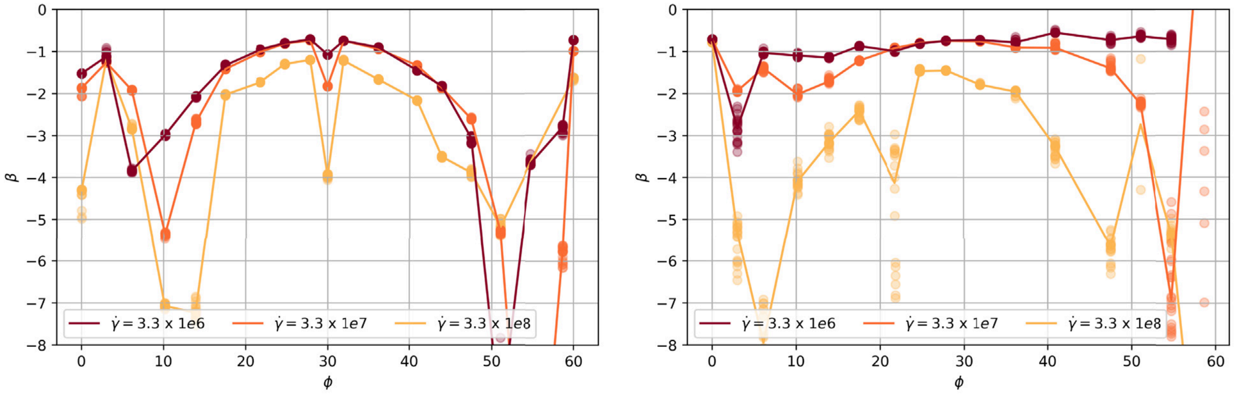

(a) T = 600 K

(b) T=900K

Fig. 12. Coupling factors for $\Sigma 7[1\,1\,1]$ GBs for different shear rates. See caption to Fig. 9, which describes the relationship between the scattered data and the line plots. The 0° and 60° inclination angles correspond to the $\Sigma 7[1\,1\,1](1\,4\,\bar{5})$ STGB, and 30° represents the $\Sigma 7[1\,1\,1](2\,1\,\bar{3})$ STGB.

similar coupling factor as that of the STGB (see Figs. 12(a) and 12(b)). This trend was not heavily affected by changes to the shear rate. Similar observations hold for $\Sigma 21[1\,1\,1]$ ATGBs in the neighborhood of 0° or 60° STGBs.

As was the case with shear rate, the coupling factors of $\Sigma 7[1\,1\,1]$ ATGBs in the neighborhood of the 30° inclination angle STGB are insensitive to an increase in temperature. For the rest of the inclination angles in the $\Sigma 7$ case, however, the scatter in the time-dependent

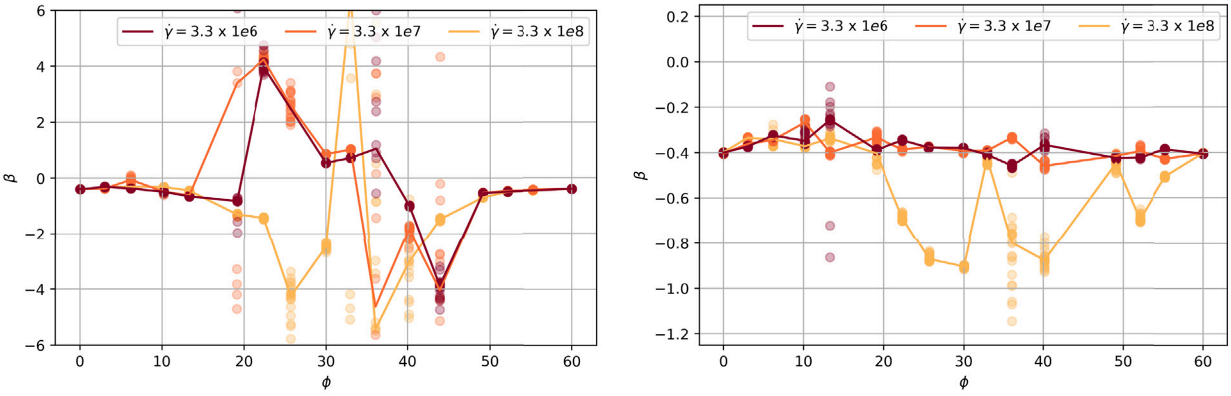

(a) T = 600 K

(b) T=900K

Fig. 13. Coupling factors for $\Sigma 21[1\,1\,1]$ GBs for different shear rates. See caption to Fig. 9, which describes the relationship between the scattered data and the line plots. The 0° and 60° inclination angles correspond to the $\Sigma 21[1\,1\,1](1\,2\,\bar{3})$ STGB, and 30° angle represents the $\Sigma 21[1\,1\,1](4\,1\,\bar{5})$ STGB.

coupling factor data and the magnitude of their median increase with temperature as expected. On the other hand, the scatter and the magnitude of the coupling factors in the $\Sigma 21[1\,1\,1]$ case were observed to decrease with an increase in temperature across all simulated inclinations. This trend can be easily seen in supplementary Figure 10, where the coupling factor converges much quicker and consistently at higher temperature. This is in contrast to the commonly reported behavior of grain boundaries, where an increase in temperature in the range $0.2T_m < T < 0.8T_m$ (T_m - melting temperature) leads to an increase in the coupling factor [39].

[1 1 0] *ATGBs*

We end this section with results on $\Sigma 9[1\,1\,0]$ and $\Sigma 11[1\,1\,0]$ ATGBs. Materials with low stacking-fault energies (e.g. Cu) tend to favor non-GB-mediated mechanisms over shear coupling in [1 1 0] ATGBs, making them less ideal for studying shear coupling behavior. Al is an ideal candidate in this regard due to its high stacking-fault energy (and obvious relevance as a structural materials), but it has a low melting point that results in ATGB premelting. Therefore, we report in Figs. 14 and 15 only the $T = 600\,\mathrm{K}$ case. Figs. 14 and 15 show that the shear coupling behavior was the most erratic in the [110] ATGBs compared to the other tilt axes studied in this paper.

3.2. Results from the discrete disconnection model

Using the discrete disconnection model of Section 2.3, we calculated the expected coupling factors for all GB systems listed in Table 1. Figs. 16 to 18 show the coupling factors from the discrete disconnection model in blue. The plots in red correspond to the coupling factors obtained from MD simulations at 600 K and at a shear rate of $\approx 1\times 10\ \mathrm{s}^{-1}$, and the gray points refer to the coupling factors of the enumerated disconnections.

The coupling factors predicted by the discrete disconnection model do not match the coupling factors observed in MD simulations. The predicted high variation in coupling factors, even for small angle changes, is because the coupling factors of the individual disconnection modes (shown in gray in Figs. 16 to 17) exhibit a similar trend, which can be attributed to the discrete nature of the lattices. This is analogous to the large variations in Σ for small misorientation changes.

The above observation brings into focus the flatness assumption (A1) (see Section 2.3). If an ATGB were allowed to equilibrate in an MD simulation, it is well-known that the lattices relax by nucleating *intrinsic disconnection dipoles* which either manifest as atomic-sized steps or facets. Since intrinsic disconnections do not alter the macroscopic degrees of freedom, they represent a GB microstate. The intrinsic disconnections in an ATGB tend to transform most of the boundary to a neighboring (in the inclination space) low-energy GB and the defect content accounts for the inclination angle difference with the low-energy GB. Therefore, intrinsic disconnections regularize the variations in the structure of ATGBs with respect to small angle changes. Intrinsic disconnections also occur in STGBs with misorientation angles close to that of an energetically favorable low Σ STGB. The intrinsic disconnections in such cases exist to account for the deviation from the energetically favorable low Σ STGB. Since the coupling factors of STGBs, predicted by the mesoscale model, do not show much scatter [13], the effect of intrinsic disconnections on the coupling factor was not as critical to STGBs as to ATGBs. Therefore, mitigating the above drawbacks of the mesoscale model in ATGBs necessitates incorporating the effect of intrinsic disconnection dipoles. However, as the intrinsic disconnections occur at the atomic scale and our interest is in the mesoscale, we do not want to explicitly track them. One strategy is to recognize that the effect of intrinsic disconnections, in addition to atomic shuffles, will manifest on the disconnection nucleation barriers. Therefore, we postulate that computing disconnection nucleation barriers more accurately at the atomic scale, as opposed to the currently used classical nucleation model of Khater et al. [12], will greatly improve the predictions of the mesoscale model.

4. Conclusion

In this paper, we carried out an extensive survey of the shear coupling of ATGBs using MD simulations at the atomic scale and a discrete disconnection model at the mesoscale. More specifically, shear coupling factors of 244 ATGBs spanning multiple misorientation angles and three tilt axes were measured in Cu and Al bicrystals subjected to temperatures and strain rates that span three orders of magnitude. MD simulations reveal that the mechanisms behind the shear coupling are relatively more complex in ATGBs compared to STGBs and are sensitive to shear rate. The latter feature was based on the observation that some ATGBs curve as they migrate, and as a result, experience localized stress concentration. However, the curvature decreases for lower strain rates, highlighting rate dependence. In addition, the dependence of the coupling factor on the inclination angle is highly nonlinear compared to the relatively simple piecewise linear dependence on the misorientation angle of STGBs. While variations (along the GB) in the coupling factor and its magnitude increased with temperature and strain rates in most ATGBs, certain exceptions were noted. While some [001] ($\Sigma 25$ and $\Sigma 13$) and [111] tilt axis ATGBs show symmetry in coupling factors in accordance to the symmetry in atomic structure (bicrystallography are symmetric about 45° for [001] tilt axis and 30° for [111] tilt axis),

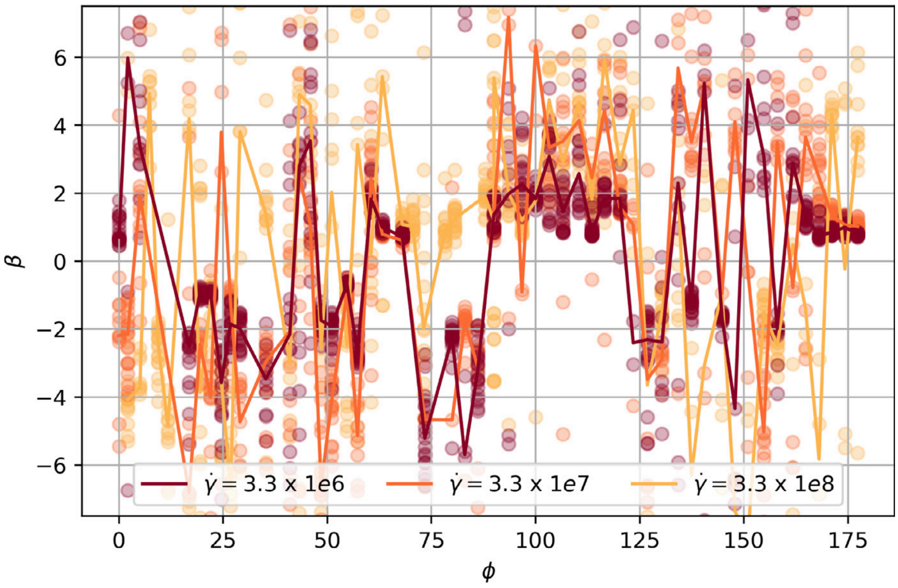

Fig. 14. Coupling factors for $\Sigma 9[1\,1\,0]$ GBs for different shear rates. See caption to Fig. 9, which describes the relationship between the scattered data and the line plots. The 0° and 180° inclination angles correspond to the $\Sigma 9[1\,1\,0](1\,\bar{1}\,4)$ STGB, while 90° corresponds to $\Sigma 9[1\,1\,0](2\,\bar{2}\,1)$ STGB.

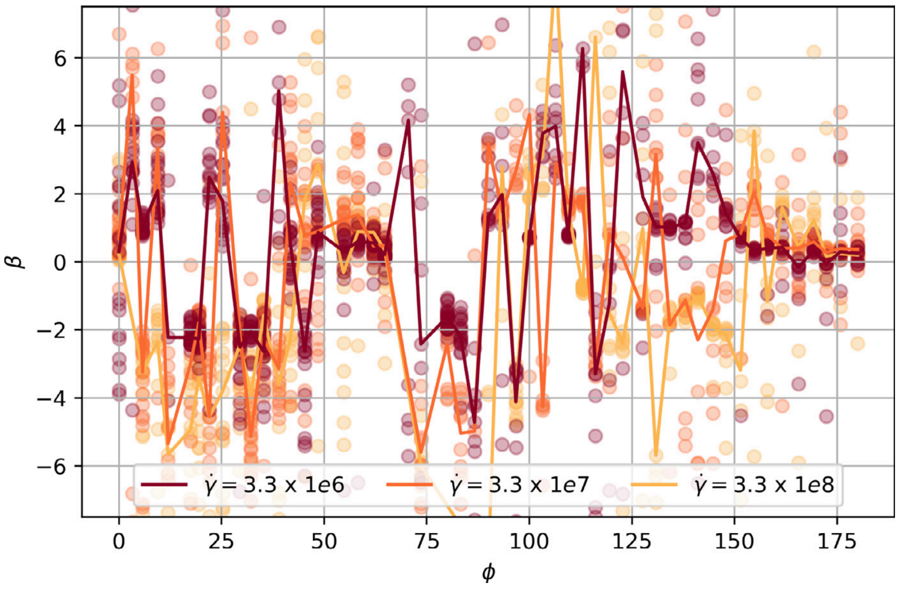

Fig. 15. Coupling factors for $\Sigma 11[1\,1\,0]$ GBs for different shear rates. See caption to Fig. 9, which describes the relationship between the scattered data and the line plots. The 0° and 180° inclination angles correspond to the $\Sigma 11[1\,1\,0](1\,\bar{1}\,3)$ STGB, while 90° corresponds to $\Sigma 11[1\,1\,0](3\,\bar{3}\,2)$ STGB.

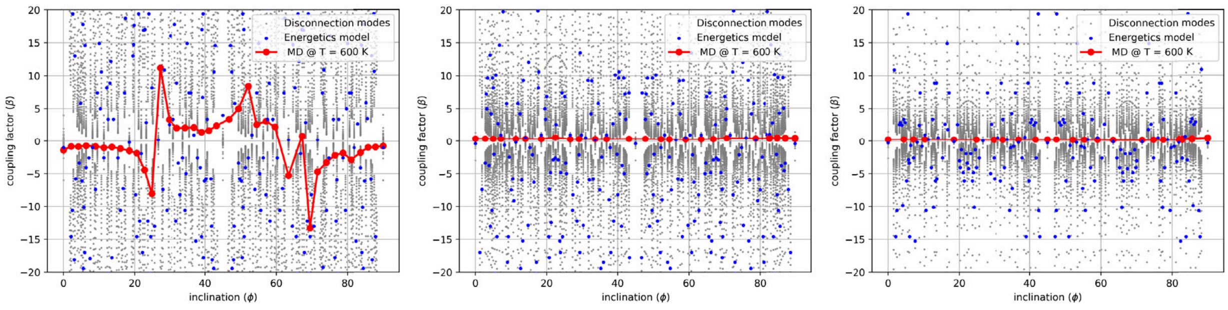

(a) Σ5[0 0 1]

(b) Σ13[0 0 1]

(c) Σ25[0 0 1]

Fig. 16. A comparison of coupling factors of [001] ATGBs calculated using the discrete disconnection model (blue) with those observed in MD simulations (red). The gray points show the coupling factors of individual disconnection modes in a [001] ATGB. (For interpretation of the references to color in this figure legend, the reader is referred to the web version of this article.)

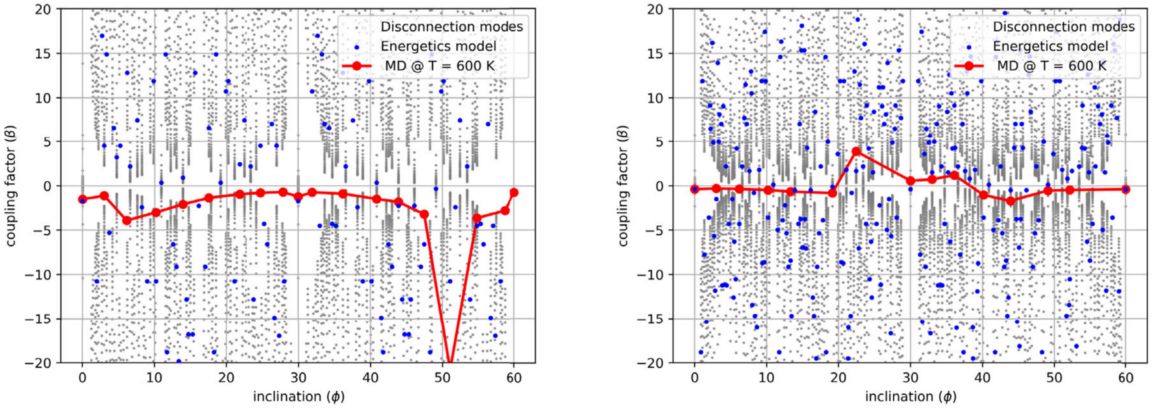

(a) Σ7[1 1 1] (b) Σ21[1 1 1]

Fig. 17. A comparison of coupling factors of [111] ATGBs calculated using the discrete disconnection model (blue) with those observed in MD simulations (red). The gray points show the coupling factors of individual disconnection modes in a [111] ATGB. (For interpretation of the references to color in this figure legend, the reader is referred to the web version of this article.)

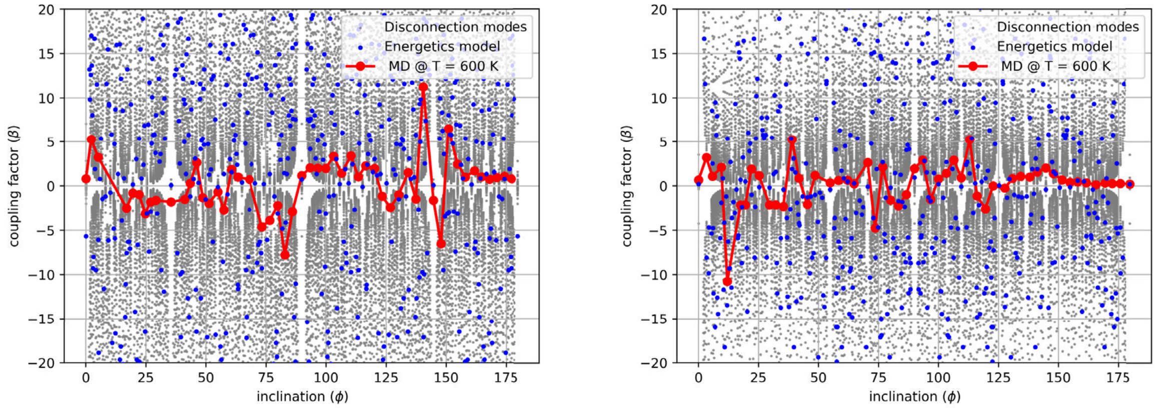

(a) Σ9[1 1 0] (b) Σ11[1 1 0]

Fig. 18. A comparison of coupling factors of [110] ATGBs calculated using the discrete disconnection model (blue) with those observed in MD simulations (red). The gray points show the coupling factors of individual disconnection modes in a [110] ATGB. (For interpretation of the references to color in this figure legend, the reader is referred to the web version of this article.)

this is not true in general. $\Sigma5[001]$ and [110] ATGBs do not show such symmetry. This can be attributed to the microstates that are available to the ATGBs, and requires further investigation.

Motivated by the recent work of Han et al. [13], we extended the mesoscale model of Khater et al. [12] to ATGBs to predict the trends observed in our MD simulations. The mesoscale model relied on four key assumptions: (a) a GB is a perfectly flat interface and continues to remain flat as it migrates; (b) disconnection with the smallest nucleation barrier mediates the shear coupling of a GB, with homogeneous nucleation being considered; (c) the grains adjoining a GB are elastically isotropic; and (d) shear coupling of GBs is a consequence of effective glide of disconnections along a GB, possibly mediated by climb. We demonstrated that the predictions of the mesoscale model, while working well for STGBs, do not match well with the ATGB MD results. It shows large variations in the coupling factor that originate from the discreteness of the lattice and the flatness assumption, which ignores the presence of intrinsic disconnections. With a future goal to mitigate the drawbacks of the mesoscale model, we recommend calculating the nucleation barriers of individual disconnection modes using atomistic methods, such as NEB approach taken by Rajabzadeh et al. [40].

CRediT authorship contribution statement

Himanshu Joshi: Data curation, Formal analysis, Investigation, Methodology, Software, Validation, Visualization, Writing – original draft. **Ian Chesser:** Investigation, Supervision, Writing – review & editing. **Brandon Runnels:** Investigation, Project administration, Resources, Visualization, Writing – review & editing. **Nikhil Chandra Admal:** Conceptualization, Formal analysis, Funding acquisition, Investigation, Methodology, Project administration, Software, Supervision, Writing – review & editing.

Declaration of competing interest

The authors declare that they have no known competing financial interests or personal relationships that could have appeared to influence the work reported in this paper.

Acknowledgments

NCA and HJ would like to acknowledge support from the National Science Foundation, USA Grant NSF- MOMS-2239734. BR acknowledges support from the National Science Foundation, USA, grant No. MOMS-2142164. This work used the INCLINE cluster at the University of Colorado Colorado Springs. INCLINE is supported by the National Science Foundation, USA, grant No. 2017917.

Appendix A. Supplementary data

Supplementary material related to this article can be found online at https://doi.org/10.1016/j.actamat.2024.119994.

References

[1] M. Trudeau, J. Ying, Nanocrystalline materials in catalysis and electrocatalysis: structure tailoring and surface reactivity, Nanostruct. Mater. 7 (1–2) (1996) 245–258.

[2] R. Schulz, J. Huot, G. Liang, S. Boily, G. Lalande, M. Denis, J. Dodelet, Recent developments in the applications of nanocrystalline materials to hydrogen technologies, Mater. Sci. Eng. A 267 (2) (1999) 240–245.

[3] G. Wang, L. Sun, D. Bradhurst, S. Zhong, S. Dou, H. Liu, Nanocrystalline NiSi alloy as an anode material for lithium-ion batteries, J. Alloys Compd. 306 (1–2) (2000) 249–252.

[4] E. Lehockey, G. Palumbo, P. Lin, Improving the weldability and service performance of nickel-and iron-based superalloys by grain boundary engineering, Metall. Mater. Trans. A 29 (1998) 3069–3079.

[5] H. Fukutomi, T. Kamijo, Grain boundary sliding-migration of aluminum $<110>$ $\Sigma 11$ $\{1\,1\,3\}$ symmetric tilt coincidence grain boundary and its interpretation based on the motion of perfect DSC dislocations, Scr. Metall. 19 (2) (1985) 195–197.

[6] M. Legros, D.S. Gianola, K.J. Hemker, In situ TEM observations of fast grain-boundary motion in stressed nanocrystalline aluminum films, Acta Mater. 56 (14) (2008) 3380–3393.

[7] F. Mompiou, D. Caillard, M. Legros, Grain boundary shear-migration coupling–I. In situ TEM straining experiments in Al polycrystals, Acta Mater. 57 (7) (2009) 2198–2209.

[8] K.D. Molodov, D.A. Molodov, Grain boundary mediated plasticity: On the evaluation of grain boundary migration-shear coupling, Acta Mater. 153 (2018) 336–353.

[9] E.R. Homer, S.M. Foiles, E.A. Holm, D.L. Olmsted, Phenomenology of shear-coupled grain boundary motion in symmetric tilt and general grain boundaries, Acta Mater. 61 (4) (2013) 1048–1060.

[10] S.L. Thomas, K. Chen, J. Han, P.K. Purohit, D.J. Srolovitz, Reconciling grain growth and shear-coupled grain boundary migration, Nature Commun. 8 (1) (2017) 1–12.

[11] Q. Zhu, G. Cao, J. Wang, C. Deng, J. Li, Z. Zhang, S.X. Mao, In situ atomistic observation of disconnection-mediated grain boundary migration, Nature Commun. 10 (1) (2019) 1–8.

[12] H. Khater, A. Serra, R. Pond, J. Hirth, The disconnection mechanism of coupled migration and shear at grain boundaries, Acta Mater. 60 (5) (2012) 2007–2020.

[13] J. Han, S.L. Thomas, D.J. Srolovitz, Grain-boundary kinetics: A unified approach, Prog. Mater. Sci. 98 (2018) 386–476.

[14] D. Singh, A. Parashar, Effect of symmetric and asymmetric tilt grain boundaries on the tensile behaviour of bcc-Niobium, Comput. Mater. Sci. 143 (2018) 126–132.

[15] E. Lin, H. Shi, L. Niu, E. Jin, Shock response of copper bicrystals with a $\Sigma 3$ asymmetric tilt grain boundary, Comput. Mater. Sci. 59 (2012) 94–100.

[16] X. Zhang, K. Wang, J. Chen, W. Hu, W. Zhu, S. Xiao, H. Deng, M. Cai, Shock-induced migration of asymmetry tilt grain boundary in iron bicrystal: A case study of $\Sigma 3$ $[1\,1\,0]$, Chin. Phys. B 28 (12) (2019) 126201.

[17] D. Medlin, K. Hattar, J. Zimmerman, F. Abdeljawad, S. Foiles, Defect character at grain boundary facet junctions: Analysis of an asymmetric $\Sigma=5$ grain boundary in Fe, Acta Mater. 124 (2017) 383–396.

[18] M. Tschopp, D. McDowell, Structures and energies of Σ 3 asymmetric tilt grain boundaries in copper and aluminium, Phil. Mag. 87 (22) (2007) 3147–3173.

[19] M. Tschopp, D. McDowell, Asymmetric tilt grain boundary structure and energy in copper and aluminium, Phil. Mag. 87 (25) (2007) 3871–3892.

[20] J. Brown, Y. Mishin, Dissociation and faceting of asymmetrical tilt grain boundaries: Molecular dynamics simulations of copper, Phys. Rev. B 76 (13) (2007) 134118.

[21] J.-P. Couzinié, O. Hardouin Duparc, S. Lartigue-Korinek, J. Thibault-Pénisson, B. Décamps, L. Priester, On the atomic structure of an asymmetrical near $\Sigma = 27$ grain boundary in copper, Phil. Mag. Lett. 89 (12) (2009) 757–767.

[22] L. Kar'kina, I. Kar'kin, Y.N. Gornostyrev, Grain boundary sliding along special asymmetric grain boundaries in the Al Bicrystals: Atomistic molecular dynamics simulation, Phys. Met. Metallogr. 122 (11) (2021) 1103–1111.

[23] Z. Trautt, A. Adland, A. Karma, Y. Mishin, Coupled motion of asymmetrical tilt grain boundaries: Molecular dynamics and phase field crystal simulations, Acta Mater. 60 (19) (2012) 6528–6546.

[24] S. Fensin, M. Asta, R. Hoagland, Temperature dependence of the structure and shear response of a $\Sigma 11$ asymmetric tilt grain boundary in copper from molecular-dynamics, Phil. Mag. 92 (34) (2012) 4320–4333.

[25] L. Zhang, C. Lu, K. Tieu, X. Zhao, L. Pei, Shear response of copper bicrystal with $\Sigma 11$ symmetric and asymmetric tilt grain boundaries by molecular dynamics simulation, Nanoscale 7 (2015) 7224–7233, http://dx.doi.org/10.1039/C4NR07496C.

[26] E. Guleryuz, S.D. Mesarovic, Dislocation nucleation on grain boundaries: low angle twist and asymmetric tilt boundaries, Crystals 6 (7) (2016) 77.

[27] T. Shimokawa, T. Kinari, S. Shintaku, Interaction mechanism between edge dislocations and asymmetrical tilt grain boundaries investigated via quasicontinuum simulations, Phys. Rev. B 75 (14) (2007) 144108.

[28] L. Wan, J. Li, Shear responses of $[\bar{1}\,1\,0]$-tilt $\{1\ 1\ 5\}/\{1\ 1\ 1\}$ asymmetric tilt grain boundaries in fcc metals by atomistic simulations, Modelling Simul. Mater. Sci. Eng. 21 (5) (2013) 055013.

[29] N.C. Admal, T. Ahmed, E. Martinez, G. Po, Interface dislocations and grain boundary disconnections using smith normal bicrystallography, Acta Mater. 240 (2022) 118340.

[30] Y. Mishin, M. Mehl, D. Papaconstantopoulos, A. Voter, J. Kress, Structural stability and lattice defects in copper: Ab initio, tight-binding, and embedded-atom calculations, Phys. Rev. B 63 (22) (2001) 224106.

[31] X.W. Zhou, R.A. Johnson, H.N.G. Wadley, Misfit-energy-increasing dislocations in vapor-deposited CoFe/NiFe multilayers, Phys. Rev. B 69 (2004) 144113, http://dx.doi.org/10.1103/PhysRevB.69.144113, URL: https://link.aps.org/doi/10.1103/PhysRevB.69.144113.

[32] A.P. Thompson, H.M. Aktulga, R. Berger, D.S. Bolintineanu, W.M. Brown, P.S. Crozier, P.J. in 't Veld, A. Kohlmeyer, S.G. Moore, T.D. Nguyen, R. Shan, M.J. Stevens, J. Tranchida, C. Trott, S.J. Plimpton, LAMMPS - a flexible simulation tool for particle-based materials modeling at the atomic, meso, and continuum scales, Comp. Phys. Comm. 271 (2022) 108171, http://dx.doi.org/10.1016/j.cpc.2021.108171.

[33] A. Stukowski, Visualization and analysis of atomistic simulation data with OVITO-the Open Visualization Tool, Modelling Simul. Mater. Sci. Eng. (ISSN: 0965-0393) 18 (1) (2010) http://dx.doi.org/10.1088/0965-0393/18/1/015012.

[34] Y. Deng, C. Deng, Size and rate dependent grain boundary motion mediated by disconnection nucleation, Acta Mater. 131 (2017) 400–409.

[35] Q. Zhu, H. Zhou, Y. Chen, G. Cao, C. Deng, Z. Zhang, J. Wang, Atomistic dynamics of disconnection-mediated grain boundary plasticity: A case study of gold nanocrystals, J. Mater. Sci. Technol. 125 (2022) 182–191.

[36] K. Chen, J. Han, X. Pan, D.J. Srolovitz, The grain boundary mobility tensor, Proc. Natl. Acad. Sci. 117 (9) (2020) 4533–4538.

[37] M.A. Tschopp, S.P. Coleman, D.L. McDowell, Symmetric and asymmetric tilt grain boundary structure and energy in Cu and Al (and transferability to other fcc metals), Integrating Mater. Manuf. Innov. 4 (1) (2015) 176–189.

[38] H. Joshi, I. Chesser, B. Runnels, N. Admal, An atomistic survey of shear coupling in asymmetric tilt grain boundaries and interpretation using the disconnections framework, 2024, http://dx.doi.org/10.17632/vxkg8tz8kh.1.

[39] J.W. Cahn, Y. Mishin, A. Suzuki, Coupling grain boundary motion to shear deformation, Acta Mater. 54 (19) (2006) 4953–4975.

[40] A. Rajabzadeh, F. Mompiou, M. Legros, N. Combe, Elementary mechanisms of shear-coupled grain boundary migration, Phys. Rev. Lett. 110 (26) (2013) 265507.